Ferromagnetism triggered by band tripling in ruthenate $Sr_4Ru_3O_{10}$

N. Watanabe,[1] S. Souma,[2,3,*] K. Nakayama,[1,4] K. Yamauchi,[5] J. F. Ribeiro,[2,6] Y. Wang,[7] Miho Kitamura,[8,9] Koji Horiba,[9] Hiroshi Kumigashira,[10] T. Oguchi,[5] Z. Q. Mao,[7] Y. P. Chen,[2,3,6,11] and T. Sato[1,2,3,12,13,†]

[1]*Department of Physics, Graduate School of Science, Tohoku University, Sendai 980-8578, Japan*
[2]*Advanced Institute for Materials Research (WPI-AIMR), Tohoku University, Sendai 980-8577, Japan*
[3]*Center for Science and Innovation in Spintronics (CSIS), Tohoku University, Sendai 980-8577, Japan*
[4]*Precursory Research for Embryonic Science and Technology (PRESTO), Japan Science and Technology Agency (JST), Tokyo 102-0076, Japan*
[5]*Center for Spintronics Research Network (CSRN), Osaka University, Toyonaka, Osaka 560-8531, Japan*
[6]*School of Electrical and Computer Engineering and Birck Nanotechnology Center, Purdue University, West Lafayette, Indiana 47907, USA*
[7]*Department of Physics, Pennsylvania State University, University Park, Pennsylvania 16802, USA*
[8]*Institute of Materials Structure Science, High Energy Accelerator Research Organization (KEK), Tsukuba, Ibaraki 305-0801, Japan*
[9]*National Institutes for Quantum Science and Technology (QST), Sendai 980-8579, Japan*
[10]*Institute of Multidisciplinary Research for Advanced Materials (IMRAM), Tohoku University, Sendai 980-8577, Japan*
[11]*Department of Physics and Astronomy and Purdue Quantum Science and Engineering Institute, Purdue University, West Lafayette, Indiana 47907, USA*
[12]*International Center for Synchrotron Radiation Innovation Smart (SRIS), Tohoku University, Sendai 980-8577, Japan*
[13]*Mathematical Science Center for Co-creative Society (MathCCS), Tohoku University, Sendai 980-8577, Japan*

(Received 8 January 2024; accepted 18 September 2024; published 15 October 2024)

Itinerant ferromagnetism is understood in terms of a quasiparticle picture with renormalized many-body effects. While the ferromagnetic ground state is destabilized by thermal and quantum fluctuations leading to exotic states such as unconventional superconductivity, how the quasiparticles evolve across the ferromagnetic transition is a target of intensive debate. Here, we present a type of ferromagnetic transition that is accompanied by a drastic reconstruction of quasiparticle spectrum in a layered ferromagnetic ruthenate, $Sr_4Ru_3O_{10}$. Angle-resolved photoemission spectroscopy uncovered that the three-dimensional coherent states below the ferromagnetic transition temperature (T_C) turn into two-dimensional incoherent electronic states slightly above T_C characterized by the disappearance of trilayer band splitting, ferromagnetic exchange splitting, and long-lived quasiparticles. Our findings suggest that the electronic coherence strongly modifies the fermiology and magnetic order, pointing to an intriguing coupling between quasiparticles and magnetic properties.

DOI: 10.1103/PhysRevB.110.155134

I. INTRODUCTION

Ferromagnetism is a quantum phenomenon in which exchange interaction between electron spins originating from the Coulomb repulsion and the Pauli exclusion principle [1] plays a role. In insulators, the exchange interaction between localized electrons is considered (Heisenberg picture), while in metals, itinerant quasiparticle bands dressed by the electron-electron interactions characterize the ferromagnetism (Stoner picture) [2–4]. In the latter case, since the exchange interaction is incorporated into a mean-field potential, spontaneous magnetization emerges depending on the difference in the occupancy of spin-up and spin-down bands. The exchange splitting is expected to decrease upon increasing temperature until spontaneous magnetization disappears at the Curie temperature (T_C), whereas only a few materials were found to follow this simple Stoner picture. For instance, in a typical ferromagnet such as Fe, the exchange splitting persists slightly above T_C due to residual short-range order [5,6]. In some kagome ferromagnets, no clear temperature evolution of the quasiparticle bands was observed across T_C, although the existence of flat bands (high density of states) around the Fermi level (E_F) favors the Stoner picture [7]. Intriguingly, deviation from the Stoner picture was widely recognized in many other systems, such as two-dimensional (2D) van der Waals metallic ferromagnets [8,9], itinerant weak ferromagnets [10,11], and giant magnetoresistance (GMR) compounds [12,13]. While the ferromagnetic (FM) ground state is well captured by the density functional theory (DFT) calculations in many cases, the spectral evolution of the quasiparticles across the FM transition poses a long-standing theoretical challenge [14,15]. Experimentally unveiling the quasiparticle nature across the FM transition is of significant importance, since exotic phenomena such as unconventional superconductivity and quantum critical behavior appear in proximity to the FM phase [16,17].

Here we focus on the Ruddlesden-Popper-phase ruthenates $Sr_{n+1}Ru_nO_{3n+1}$ (SRO; n is the number of RuO_2 planes

*Contact author: s.souma@arpes.phys.tohoku.ac.jp
†Contact author: t-sato@arpes.phys.tohoku.ac.jp

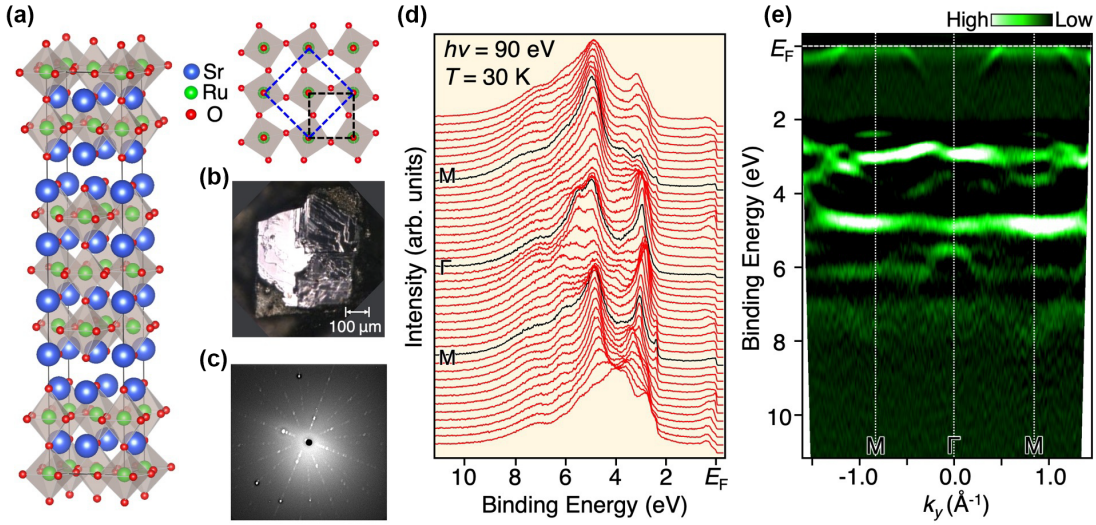

FIG. 1. (a) Crystal structure of Ruddlesden-Popper phase ruthenate $Sr_{n+1}Ru_nO_{3n+1}$ ($n = 3$) and (right) schematics of the rotation of RuO_6 octahedra. Blue and black dashed squares correspond to the unit cell with and without the octahedral rotation, respectively. (b),(c) Typical photograph and x-ray Laue backscattering image of $S_4Ru_3O_{10}$ single crystal, respectively. (d) EDCs in a wide binding-energy range for SRO ($n = 3$) measured along the ΓM cut at $T = 30$ K with $h\nu = 90$ eV. (e) Corresponding ARPES intensity plot obtained by taking the second derivative of EDCs in (d).

in a unit cell) consisting of periodically stacked conducting RuO_2 planes and SrO block layers to address the quasiparticles in the FM state. The SRO family serves as a good test-bed system in which one can study the interplay between quasiparticles and ferromagnetism under strong electron correlation. Infinite-layer $SrRuO_3$ ($n = \infty$) with cubic structure is a ferromagnet with $T_C = 160$ K [18,19], and the ferromagnetism is still kept down to $n = 3$ although the T_C is reduced to 105 K [20,21]. $n = 2$ is located near the boundary of the FM phase, since metamagnetism and a quantum critical point appear [22]. The Fermi surface of SRO consists of multiple Ru $4d$ t_{2g} orbitals, and low-energy excitations are characterized by mass-renormalized quasiparticles as revealed by angle-resolved photoemission spectroscopy (ARPES) and thermodynamic measurements [23–26].

So far, the experimental investigations on electronic states of SRO have been mainly focused on $n = 1$ and 2 [23–35], with a few studies for $n = \infty$ [36–39]. In particular, the electronic states of $n = 1$ and 2 have been intensively studied by ARPES [25,26,28–30,32,34,35], quantum oscillations [23,31], and DFT calculations [27,32,33]. These studies commonly pointed out the importance of multiple orbitals and band reconstruction associated with the rotation of an RuO_6 octahedron [30,32,34,40]. On the other hand, for $n = 3$ showing ferromagnetism [$Sr_4Ru_3O_{10}$; see Fig. 1(a) for the crystal structure], only a limited number of experimental studies have been hitherto reported [33,41–43]. While the existence of quasiparticle peaks in the excitation spectra has been also suggested in $n = 3$ [43], the interplay between quasiparticles and ferromagnetism, which can be investigated at $n = 3$, has yet to be clarified.

In this study, we have fabricated high-quality $Sr_4Ru_3O_{10}$ single crystal using the floating-zone technique, and we succeeded in selectively probing a small but flat and clean region of a cleaved surface [typical photographs of the cleaved surface and the x-ray Laue image are shown in Figs. 1(b) and 1(c), respectively] by utilizing a micro (μ) focused beam spot in ARPES measurements that achieves a drastically improved momentum (k) resolution. The μ-ARPES plays a key role in resolving a band splitting associated with the interlayer coupling and the FM exchange interaction.

II. EXPERIMENT AND CALCULATION

$Sr_4Ru_3O_{10}$ single crystals were grown using the floating-zone technique, and detailed growth conditions were reported in Ref. [44]. T_C of the sample was estimated as 105 K from the magnetization measurement. μ-ARPES measurements were performed with a Scienta-Omicron DA30 electron analyzer with microfocused synchrotron light at BL-28A in Photon Factory [45]. We used circularly/linearly polarized light of $h\nu = 90$ eV. This photon energy was found to be useful to clearly resolve the band splitting. The energy resolution was set to be 10–30 meV. Samples were cleaved *in situ* in an ultrahigh vacuum of 1×10^{-10} Torr and kept at $T =$ 20–160 K during the measurements. First-principles band-structure calculations were carried out by using a projector augmented wave method implemented in Vienna Ab initio Simulation Package (VASP) code [46] with the generalized gradient approximation (GGA). Starting with the experimentally observed *Pbam* crystal structure [20], the internal atomic coordinates were optimized until forces acting on atoms were smaller than 1×10^{-5} eV/Å. The total energy was calculated self-consistently with the tetrahedron sampling of a $8 \times 8 \times 1$ k-point mesh. Spin-orbit coupling was taken into account in the calculation. The Fermi lines were drawn by using the FERMISURFER program [47].

III. RESULTS AND DISCUSSION

At first, we present the overall valence-band structure of $Sr_4Ru_3O_{10}$. Figure 1(d) displays the energy distribution

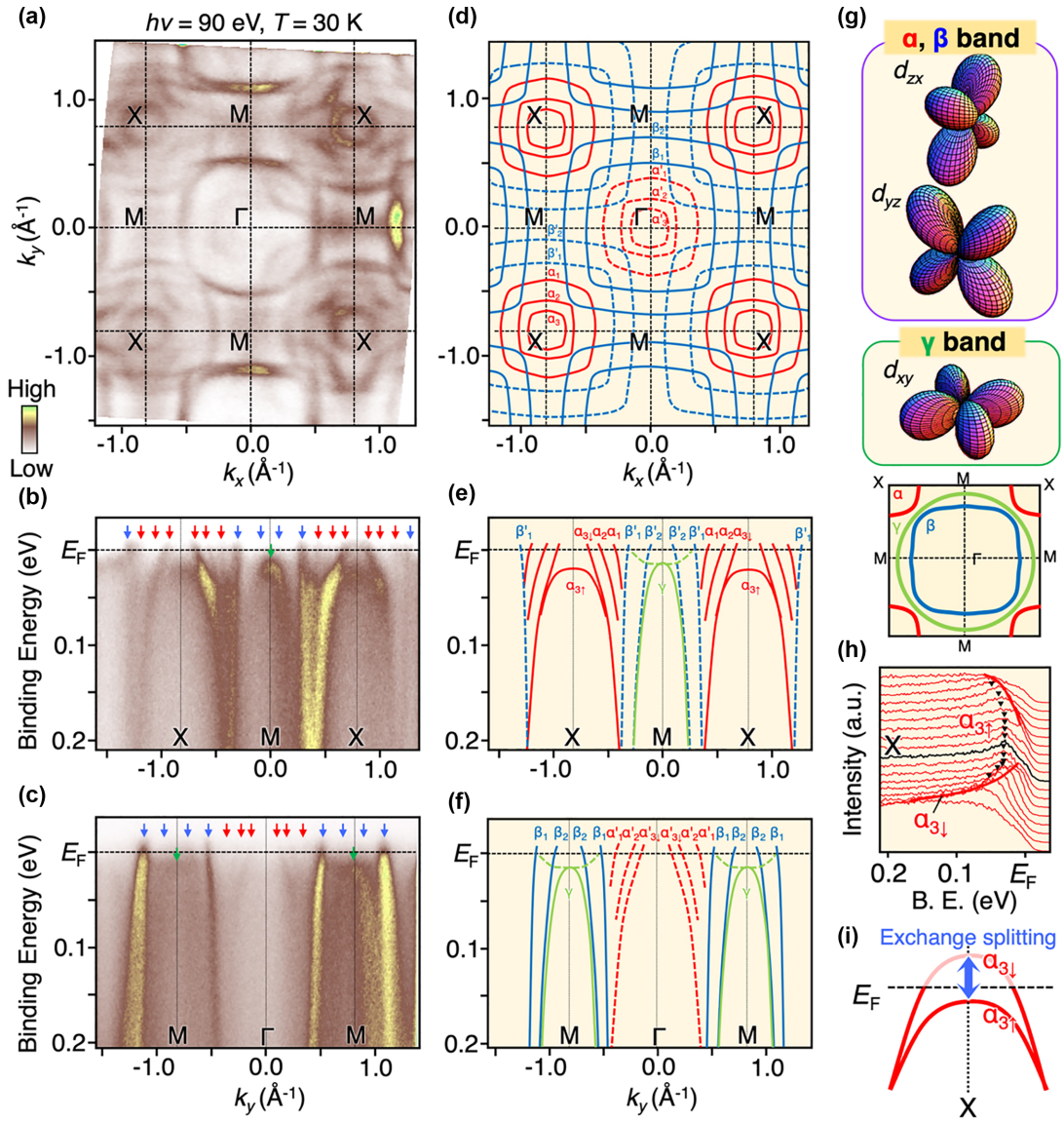

FIG. 2. (a) ARPES intensity at E_F for SRO ($n = 3$) measured at $T = 30$ K plotted as a function of in-plane wave vector k_x and k_y obtained with $h\nu = 90$ eV. (b), (c) Near-E_F ARPES intensity along the XM and ΓM cuts, respectively. (d) Schematic experimental Fermi surface obtained by tracing the k_F points in (a). (e), (f) Schematic experimental band dispersions along the XM and ΓM cuts, respectively, obtained by tracing the peak position of EDCs/MDCs. Red, blue, and green curves in (d)–(f) correspond to the Fermi surfaces/band dispersions of the α, β, and γ bands, respectively. (g) Schematic wave functions for Ru d_{zx}, d_{yz}, and d_{xy} orbital. The bottom panel shows the schematic Fermi surface for $n = 1$. (h) EDCs near E_F around the X point. Triangles and red curves trace the dispersion of $\alpha_{3\uparrow}$, and $\alpha_{3\downarrow}$ bands, respectively. (i) Schematic band diagram of exchange-split α_3 bands near E_F.

curves (EDCs) in the wide binding-energy (E_B) region measured along the ΓM cut of the 1×1 (without octahedral rotation) Brillouin zone (BZ) in the FM phase ($T = 30$ K). One can identify several dispersive bands with a dominant intensity at $E_B \sim 2$–8 eV, together with weaker features dispersing within $\sim$1 eV of E_F. They are attributed to the O $2p$ orbital and Ru $4d$ quasiparticle bands, respectively [27–29], and they are better visualized in the second-derivative intensity plot in Fig. 1(e).

In Fig. 2(c), one can also recognize two highly dispersive bands outside the Γ-centered α_1' pocket. They are attributed to the two β bands, β_1 and β_2 (blue arrows). As shown in Fig. 2(a), the β_1 band forms a large squarelike Fermi surface centered at the Γ point outside the outer pocket α_1', and the β_2 band forms an even larger square pocket also centered at the Γ point [see also Fig. 2(d)]. Corresponding replica bands due to the band folding appear as the β_1' and β_2' bands (blue dashed curves) in the ARPES intensity along the XM cut [Figs. 2(b) and 2(e)] and the Fermi-surface mapping [Figs. 2(a) and 2(d)]. The multiple character of α and β bands and corresponding replica bands, as represented by the presence of three α bands, suggests that they are caused by the trilayer band splitting associated with the inter-RuO_2-layer coupling. The third β band is not clearly resolved, probably because it is too weak in the present experimental condition. The observation of trilayer splitting is also corroborated with our first-principles band-structure calculations for $n = 3$ (see Appendix A), supporting that the quasiparticle picture is a good starting point

to describe the band structure of $Sr_4Ru_3O_{10}$ in the FM phase. Since the trilayer band splitting in layered compounds has been observed so far only in cuprate ($Bi_2Sr_2Ca_2Cu_3O_{10}$) [48], the present result adds a second concrete material case. A key to resolve the trilayer splitting is the utilization of μ-ARPES, which greatly improves the k resolution (see Appendix B).

A careful look at the ARPES intensity in Fig. 2(b) reveals the existence of an additional band topped at 15 meV below E_F at the M point (marked by a green arrow). This band forms a van Hove singularity at the M point (see Appendix C) and is assigned to the γ band whose singularity point is located above E_F for $n = 1$ [25,26,30,34,35] and slightly below E_F for $n = 2$. This has been discussed as the origin of metamagnetism [32]. Interestingly, we do not resolve a clear trilayer splitting for the γ band unlike the case of the α and β bands. The γ band has the d_{xy} orbital character [Fig. 2(g)] and its electronic wave function is elongated parallel to the RuO_2 plane. Thus, the effective interlayer hopping is reduced compared to the α and β bands with the d_{zx} and d_{yz} character, and this would lead to the very small trilayer splitting in the γ band (note that orbital assignment of the experimental bands is supported by our light-polarization-dependent ARPES measurements and first-principles calculations; see Appendix D). Such an orbital-dependent trilayer splitting is a unique feature of ruthenates with a multiorbital character, distinct from cuprates with a single-orbital ($d_{x^2-y^2}$) character. As seen in Fig. 2(b), there exists a weak feature at the X point inside the α_1–α_3 bands with the top of dispersion at $E_B \sim 20$ meV. This is better visualized in the EDCs around the X point in Fig. 2(h). Since this band shows a holelike dispersion centered at the X point as in the case of α_1–α_3 bands, it is also attributed to the α band. Taking into account the fact that (i) the trilayer splitting is expected to maximally produce three α bands, and (ii) the system is in the FM phase, this holelike band is likely produced by the FM exchange splitting of the α_3 band with the majority-spin state, called here $\alpha_{3\uparrow}$. Then, another α_3 band crossing E_F is attributed to the minority-spin state $\alpha_{3\downarrow}$ [see a schematic band diagram for the α_3 bands in Fig. 2(i)]. Thus, besides the trilayer splitting, the α bands undergo an additional splitting due to the FM exchange coupling. A reason why the exchange splitting of the α_1 and α_2 bands is not clearly resolved in the present experiment may be because their band top at which the splitting should be most clearly visible in the EDC is located much above E_F and is not accessible by ARPES. It is noted that spin-resolved ARPES measurements with a microfocused beam spot are necessary to further validate the FM exchange splitting.

The present result thus uncovers the fine band structure of $n = 3$ and provides a unified picture for the mechanism of ferromagnetism and magnetic phase diagram in SRO through a comparison of quasiparticle bands among different n's. Observation of the exchange splitting at $n = 3$ suggests itinerant Stoner-type ferromagnetism, shedding light on the debates in bulk SRO regarding the localized versus itinerant nature of ferromagnetism [36,37]. Since an essential ingredient of ferromagnetism in the Stoner model is a high density of states (DOS) around E_F, it would be reasonable to attribute the electronic states around the M and X points to the origin of the ferromagnetism, because the van Hove singularity in the γ band at the M point and the shallow pocket with a low Fermi velocity in the α band (the α_3 band for $n = 3$) at the X point are expected to largely contribute to the enhancement of the DOS around E_F. In this context, the γ band at the M point forms a van Hove singularity around E_F for both $n = 2$ [32] and 3, whereas it is away from (much above) E_F for $n = 1$ [30,34]. Regarding the shallow pocket at the X point seen for $n = 3$, it does not appear for $n = 1$ and 2 because the top of the α bands is pushed much upward into the unoccupied region [30,35]. Taking into account the fact that the spontaneous ferromagnetism appears for the first time at $n = 3$ on increasing n from $n = 1$, it is inferred that the existence of both the van Hove singularity at the M point and the shallow pocket at the X point is a key to stabilizing the ferromagnetism. In other words, besides the d_{xy} orbital (γ band), the $d_{yz/zx}$ orbital (α band) also largely contributes to the enhancement of the DOS at E_F for $n = 3$. This tendency is likely maximized for bulk cubic SRO where all the orbitals (d_{xy}, d_{yz}, d_{zx}) equally contribute to the DOS at E_F more effectively to realize the highest T_C [39,49].

Now that the electronic structure in the FM phase is established, next we present the temperature-dependent evolution of the quasiparticle bands across T_C. Figures 3(a1)–3(a8) show the near-E_F ARPES intensity along the XM cut measured at various temperatures across T_C (= 105 K). At $T = 20$ K [Fig. 3(a1)], one can recognize three α bands crossing E_F (α_1, α_2, and $\alpha_{3\downarrow}$) due to the trilayer splitting, as in Fig. 2. On the other hand, at $T = 125$ K in the paramagnetic phase [Fig. 3(a8)], one can see only a single α band with a broader intensity distribution. A detailed look at the temperature dependence of MDC at E_F in Fig. 3(b) signifies that the three peaks at $T = 20$ K associated with the k_F points of the α_1–α_3 bands gradually approach each other upon increasing temperature, still survive at 105 K (= T_C) and 115 K, and eventually merge into a single peak at $T \sim 125$ K. This behavior is supported by the quantitative analysis of MDCs; for details, see Appendix E. We have confirmed that the observed temperature-dependent band evolution is reproducible upon temperature cycle; for details, see Appendix F. These results indicate that the trilayer splitting vanishes slightly above T_C; this is unexpected from the case of a trilayer cuprate where the splitting persists in a wide temperature range including the normal state [50].

The observed unprecedented temperature evolution of the electronic structure is associated with the coherent versus incoherent behavior in low-energy excitations. According to the previous report for $n = 1$ [25], a quasiparticle peak starts to develop at $T \sim 140$ K in accordance with a sharp drop in the c-axis electrical resistivity. This was interpreted in terms of the development of coherency among RuO_2 layers. In $n = 3$, on the other hand, we found a sharp quasiparticle peak at $T = 20$ K which gradually reduces its weight and vanishes at around T_C with increasing temperature, as seen in the representative EDCs at the M point in Fig. 3(c). This supports the development of coherency at low temperature also for $n = 3$, basically in line with the resistivity data [51], which turned out to be more complex than that of $n = 1$ due to the magnetic transition. This coherency plays a crucial role in the fermiology. Namely, at high temperature, the coherent hopping among RuO_2 layers is prohibited and the effective dimensionality of the system is reduced to a 2D "single-layer"

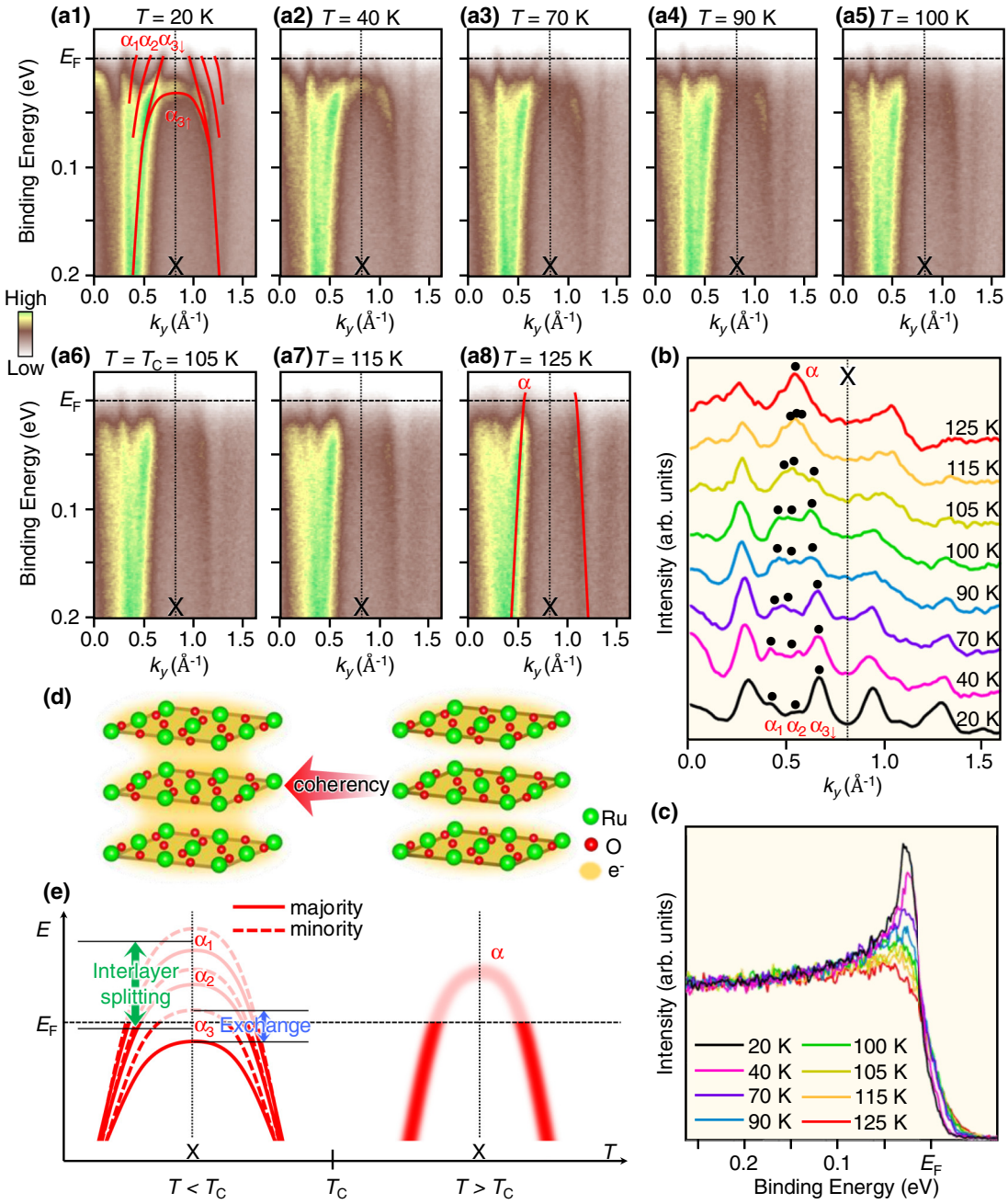

FIG. 3. (a1)–a(8) ARPES intensity along the XM cut obtained at various temperatures (T = 20–125 K) across T_C (105 K). Red curves in (a1) and (a8) trace the band dispersion of the α bands. (b) MDCs at E_F along the MX cut obtained at various temperatures (T = 20–125 K). Black dots represent the k position of the α bands estimated by the numerical fittings of MDCs with multiple Lorentzian peaks; for details, see Fig. 8 and Appendix E. (c) Temperature dependence of EDC at the X point that signifies the emergence of a quasiparticle peak below T_C. (d) Schematics of three RuO_2 planes in the unit cell which depicts incoherent (coherent) behavior above (below) T_C without (with) interlayer electron hopping. (e) Schematics of the α-band dispersion showing simultaneously the trilayer splitting due to the interlayer coupling and the exchange splitting due to the ferromagnetism (left panel). Such splitting disappears above T_C (right panel).

system in which only an incoherent (nonquasiparticle) α band exists. The top of the α band is located much above E_F [Fig. 3(e)] and does not contribute to the DOS at E_F. On the other hand, at low temperature, the development of coherency allows the interlayer hopping [Fig. 3(d)] to make the system more 3D-like, enabling the existence of quasiparticles. The resultant trilayer band splitting pushes one of the α bands (α_3) downward to enhance the DOS at E_F, triggering the ferromagnetism. Such electronic structure evolution is hard to explain in terms of a conventional Stoner picture where a large DOS at E_F that already exists well above T_C triggers the FM order. In contrast, our observation implies a more interesting situation associated with the development of the c-axis coherency [52], which simultaneously controls the interlayer hopping and ferromagnetism. We emphasize that our results are different from the Stoner ferromagnets such as Ni, where

the quasiparticle survives above T_C [53]. Our findings are also distinct from the non-Stoner-type ferromagnets such as Fe, the van der Waals magnet, and other itinerant ferromagnets [5,7,8,10,11] where the FM band splitting is unclear or persists even above T_C. Thus the present results provide a rare case of an FM transition that is correlated with the formation of quasiparticles and exchange splitting.

IV. CONCLUSION

In conclusion, we have reported ARPES results on $Sr_4Ru_3O_{10}$ and clarified the following key spectral features: (i) evidence for the triple-layer band splitting associated with the interlayer coupling, (ii) observation of exchange band splitting, which supports the itinerant ferromagnetism, and most intriguingly, (iii) disappearance of the trilayer and exchange splitting above T_C in accordance with the weakening of c-axis electronic coherence. Our results lay the foundation for understanding the interplay among dimensionality, coherent quasiparticles, and magnetic order in strongly correlated electron systems.

ACKNOWLEDGMENTS

This work was supported by JST-CREST (No. JPMJCR18T1), JST-PRESTO (No. JPMJPR18L7), JSPS (JSPS KAKENHI No. JP21H04435, No. JP24K00564, No. JP18H03858, No. JP18H04473, and No. JP20H04623), and KEK-PF (Proposals No. 2024S2-001 and No. 2021S2-001). Y.P.C. and J.F.R. also acknowledge support by WPI-AIMR and Tohoku University FRiD program. Z.Q.M. and Y.W. acknowledge the support by The Pennsylvania State University Two-Dimensional Crystal Consortium-Materials Innovation Platform (2DCC-MIP), which is supported by NSF Cooperative Agreement No. DMR-2039351.

APPENDIX A: COMPARISON OF FERMI SURFACE BETWEEN ARPES AND CALCULATION

To validate that the observed band splitting is associated with the trilayer splitting, we have performed first-principles band-structure calculations for bulk SRO ($n = 3$). The calculated Fermi surface is directly compared with the experimental Fermi surface in Fig. 4. One can recognize an overall agreement in the Fermi-surface topology between the experiment [Fig. 4(a)] and the calculation [Fig. 4(b)], in particular regarding the existence of several circular pockets centered at both Γ and X points, although the calculated Fermi surface shows very complicated fine structures. The multiple Fermi-surface pockets at the Γ and X points are produced by the trilayer splitting due to the inclusion of three RuO_2 layers in the unit cell, supporting our experimental validation of the trilayer-split Fermi surface.

APPENDIX B: COMPARISON BETWEEN REGULAR AND μ-ARPES

To demonstrate the importance of a microbeam spot in resolving the fine structure of the Fermi surface, we directly compare in Figs. 5(a) and 5(b) the ARPES intensity at E_F plotted as a function of in-plane wave vector at $T = 30$ K obtained with a regular (200×300 μm^2) and a micro (12×10 μm^2) beam spot, respectively [the spot sizes are compared in the inset to Fig. 5(a)]. One can immediately recognize an apparent difference between them; ARPES intensity obtained with the microspot [Fig. 5(b)] resolves the fine structure of the Fermi surface in great detail in contrast to that with the regular spot [Fig. 5(a)]. In particular, the trilayer-split Fermi surface is clearly seen only when we utilize the microspot. Such a difference in the sharpness of Fermi-surface mapping is likely due to the improvement of effective k resolution by (i) the reduction of the spatial integration effect of photoelectron collection in the electron analyzer, and (ii) the reduction of the quasiparticle scattering rate by effectively avoiding crystal steps on the surface.

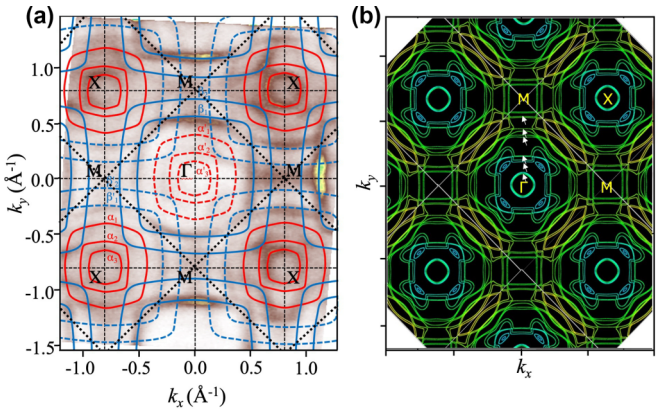

FIG. 4. (a) ARPES intensity mapping at E_F [same as Fig. 2(a)] overlapped with the experimental Fermi surface [solid curves; same as Fig. 2(d)]. (b) Calculated Fermi surface for bulk $Sr_4Ru_3O_{10}$ at the $k_z = 0$ plane in the nonmagnetic phase, obtained from the first-principles band-structure calculation, which includes the spin-orbit coupling. Possible trilayer-split α and β bands are indicated by white arrows.

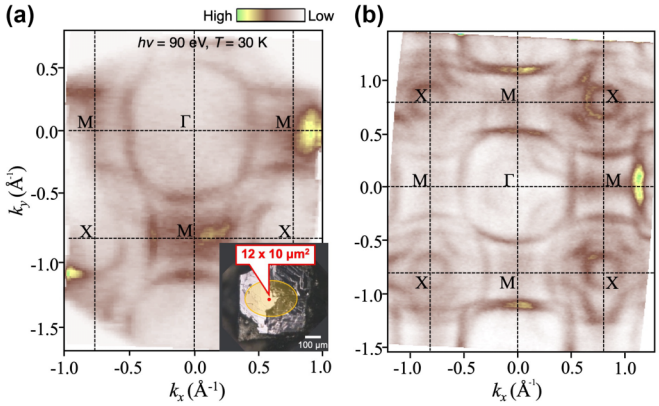

FIG. 5. (a), (b) Comparison of the Fermi-surface mapping for $n = 3$ at $T = 30$ K with $h\nu = 90$ eV between a regular beam spot ($200 \times 300\,\mu m^2$) and a microbeam spot ($12 \times 10\,\mu m^2$). The regular and microbeam spots on the cleaved sample surface are shown by yellow and red circles in the inset to (a), respectively.

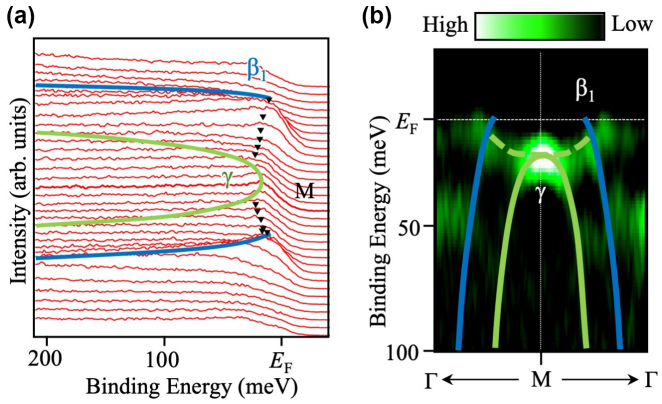

FIG. 6. (a) EDCs in the vicinity of E_F measured along the ΓM cut at $T = 30$ K, obtained with $h\nu = 90$ eV. (b) Corresponding second derivative intensity plot. Blue and green curves are a guide for the eyes to trace the band dispersion of the $\beta 1$ and γ bands. The shallow electron band is also indicated by triangles and green dashed curves in (a) and (b), respectively.

APPENDIX C: VAN HOVE SINGULARITY IN THE γ BAND

To clarify the band dispersion of the γ band and its possible contribution to the mechanism of ferromagnetism, we show the energy distribution curves (EDCs) in the vicinity of E_F around the M point at $T = 30$ K and the corresponding second derivative intensity plot in Figs. 6(a) and 6(b), respectively. Inside the $\beta 1$ band, one can see a weak holelike feature topped at the binding energy (E_B) of 15 meV [see also Figs. 2(c) and 2(f) in the main text] which is assigned to the γ band. One can also recognize a shallow electron pocket in the vicinity of E_F, whose bottom of dispersion at the M point appears to overlap with the top of the γ band to form a characteristic van Hove singularity at the M point. It is noted that a similar singular point was also seen for $n = 2$ slightly below E_F [32], whereas it is absent below E_F for $n = 1$ [30,34].

APPENDIX D: ORBITAL CHARACTER OF ENERGY BANDS

To specify the orbital character of experimentally observed energy bands, we have carried out light-polarization-dependent ARPES measurements, and the result is shown in Fig. 7. In our experimental geometry, the emission plane of photoelectrons is in the x-z plane (the x, y, and z axes are defined in the figure) corresponding to the ΓM cut in the Brillouin zone which is along the a axis, as shown in Fig. 7(a). Here we focus on the ΓM cut, because the emission plane must be perpendicular to the RuO_2 plane to simplify the discussion of the photoelectron matrix-element effect for the Ru $4d$ orbital. In our geometry, linear horizontally (LH) polarized photons whose polarization vector lies in the emission plane enhance the photoelectron intensity from the orbitals with even parity (such as the d_{zx} orbital; see the top panel) with respect to the emission plane, when we take into account the photoelectron dipole matrix element term $\langle \psi_f | A \cdot p | \psi_i \rangle$, where A, p, ψ_f, and ψ_i represent polarization vector of incident photons, the momentum of photoelectrons, and the wave functions of the final and initial states, respectively. On the other hand, linear vertically (LV) polarized photons enhance the photoelectron intensity from the orbitals with odd parity, i.e., the d_{xy} orbital (bottom panel). When the ARPES intensity along the ΓM cut is directly compared between the LH and LV photons in Figs. 7(b) and 7(c), the intensity of the γ band topped at the M point is relatively enhanced with the LV photons, whereas that of the β band outside the γ band is enhanced with the LH photons. This is consistent with our orbital assignment presented in Fig. 2 that attributed the β and γ bands to the d_{zx} and d_{xy} orbitals, respectively [note that the orbital character of the β band (d_{yz} or d_{zx}) varies depending on the wave vector, and the d_{zx} component is expected to be dominant along the ΓM cut]. To further support these arguments from the calculations, we have calculated the orbital-projected band structure by the DFT calculation, taking into account that the Fermi-surface topology between the experiment and calculation shows a reasonable agreement (Fig. 5). As shown in Fig. 7(d), one may find dispersive features along the ΓM cut corresponding to the experimental β and γ bands (highlighted by shade) despite significant complication of the band structure due to the band folding and hybridization. Importantly, the β and γ bands show overall d_{zx} and d_{xy} weights,

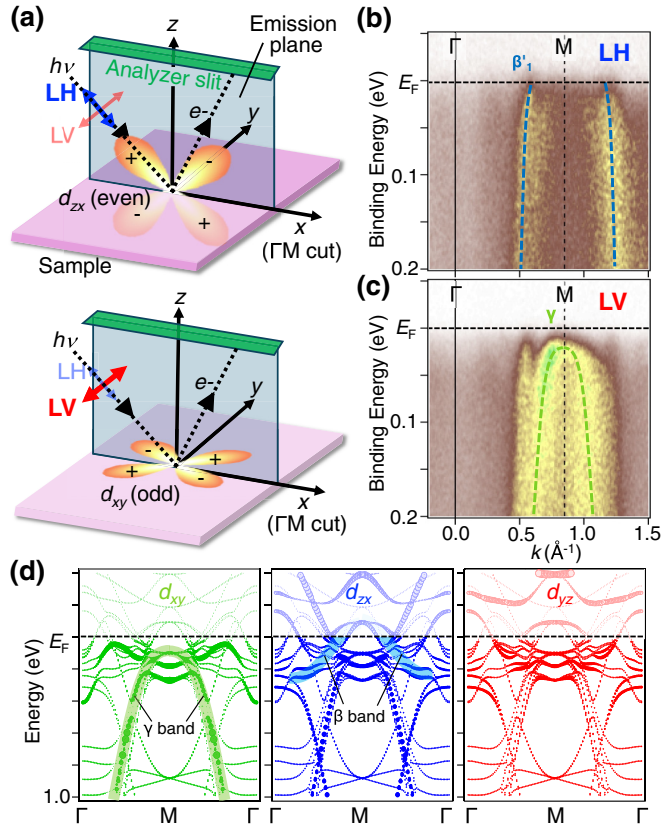

FIG. 7. (a) Schematics to show experimental geometry of the emission plane of photoelectrons, analyzer slit, light polarization (LH or LV), sample surface, and electron wave function for d_{zx} and d_{xy} orbitals. (b), (c) ARPES intensity at $T = 20$ K along the ΓM cut measured with LH and LV photons, respectively. (d) Calculated band structure along the ΓM cut. Orbital projected weights for the d_{xy}, d_{zx}, and d_{yz} orbitals are indicated by the size of circles.

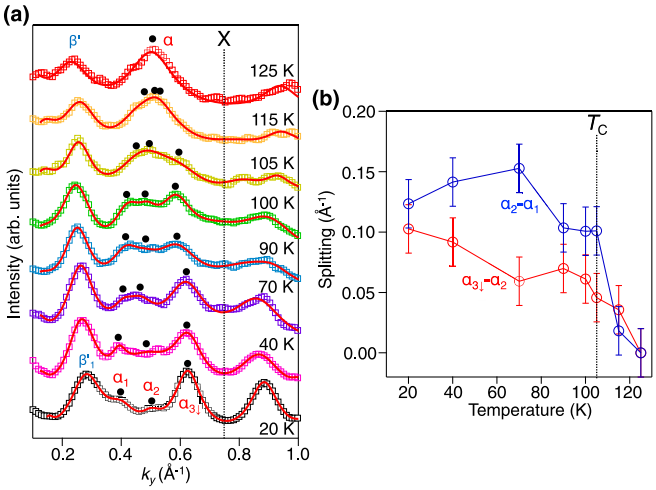

FIG. 8. (a) MDC at E_F for $n = 3$ along the XM cut at various temperatures (open squares), together with the result of numerical fittings (red curves) by assuming multiple Lorentzian peaks and a moderate background. Black dots represent the k position of Lorentzian peaks. (b) Temperature dependence of the k separation (band splitting) between the α_1 and α_2 bands as well as the $\alpha_{3\downarrow}$ and α_2 bands obtained from the numerical fittings.

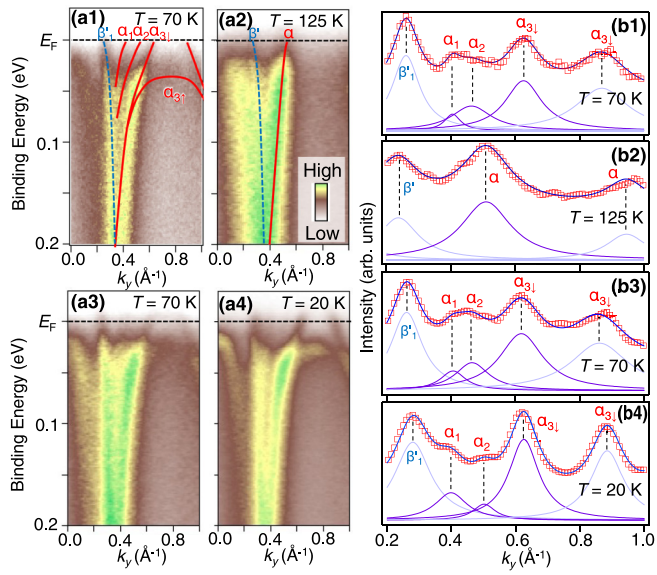

FIG. 9. (a1), (b1) ARPES intensity along the XM cut and corresponding MDC at E_F, respectively, obtained just after cleaving at $T = 70$ K. Result of numerical fittings using multiple Lorentzian peaks (red curves) together with each Lorentzian peak are shown in (b). We carried out the ARPES measurements with the following cycle: (a1), (b1) $T = 70$ K (just after cleaving) → (a2), (b2) $T = 125$ K → (a3), (b3) $T = 70$ K → (a4), (b4) $T = 20$ K.

respectively, consistent with the light-polarization-dependent ARPES measurements.

APPENDIX E: QUANTITATIVE ANALYSIS OF THE BAND SPLITTING

To show the presence of three α bands and their evolution upon temperature variation, we have numerically fitted the momentum distribution curve (MDC) at E_F by assuming multiple Lorentzian peaks along a k cut (the XM cut) where the trilayer splitting was clearly observed at low temperatures. As shown in Fig. 8(a), the MDC at $T = 20$ K is well reproduced by Lorentzian peaks for the α_1, α_2, and $\alpha_{3\downarrow}$ and folded β_1 (β'_1) bands with a moderate background, confirming trilayer splitting of the α band. Upon increasing temperature, we found that the MDCs for the α bands are well reproduced by assuming three Lorentzian peaks all the way up to 105 K (at T_C). We also found that the MDC at $T = 115$ K (10 K above T_C) cannot be perfectly fitted with a single peak but could be better fitted with three peaks with smaller k separations compared to those at low temperatures. Finally, at $T = 125$ K (20 K above T_C), the MDC was reasonably fitted by assuming a single peak within experimental uncertainties (for the spectral component of each Lorentzian peak at representative temperatures, see Fig. 9). We plot in Fig. 8(b) the temperature dependence of k separation between the α_1 and α_2 bands as well as the $\alpha_{3\downarrow}$ and α_2 bands, since they are a good measure of the magnitude of trilayer splitting. We found that the splitting seems to disappear not exactly at T_C but slightly above T_C. Based on this observation, it is expected that the counterpart of the α_3 band, i.e., the $\alpha_{3\uparrow}$ band, located at E_B of ~ 40 meV at the X point, disappears and merges into a single α band slightly above T_C. This is indeed the case when we look at the temperature dependence of EDCs at the X point in Fig. 3(b) where the spectral weight of the $\alpha_{3\uparrow}$ band monotonically reduces upon increasing temperature and finally disappears at around $T = 115$ K. Our analysis thus implies that the trilayer splitting at first sets in slightly above T_C, and after the Stoner condition is satisfied by the splitting, the system undergoes a FM transition.

APPENDIX F: REPRODUCIBILITY OF THE TEMPERATURE-DEPENDENT BAND EVOLUTION

We have confirmed that the obtained data are reproducible upon temperature cycle. As shown by the ARPES intensity and corresponding MDC at E_F in Figs. 9(a1) and 9(b1), immediately after cleaving the crystal below T_C (70 K), one can recognize trilayer-split α bands. After increasing temperature up to above T_C ($T = 125$ K), the splitting disappears [Figs. 9(a2) and 9(b2)]. After cooling the sample again to $T = 70$ K, the splitting recovers [Figs. 9(a3) and 9(b3)], and the splitting becomes more obvious at $T = 20$ K [Figs. 9(a4) and 9(b4)]. This observation supports that the disappearance of the trilayer splitting well above T_C is reproducible and is not experimental artifacts such as thermal broadening and sample aging.

[1] W. Heisenberg, On the theory of ferromagnetism, Z. Phys. **49**, 619 (1928).

[2] E. C. Stoner, Ferromagnetism, Rep. Prog. Phys. **11**, 43 (1947).

[3] E. P. Wohlfarth, The theoretical and experimental status of the collective electron theory of ferromagnetism, Rev. Mod. Phys. **25**, 211 (1953).

[4] T. Moriya, *Spin Fluctuations in Itinerant Electron Magnetism*, Springer Series in Solid-state Sciences Vol. 56 (Springer, Berlin, 1985).

[5] E. Kisker, K. Schröder, M. Campagna, and W. Gudat, Temperature dependence of the exchange splitting of Fe by spin-resolved photoemission spectroscopy with synchrotron radiation, Phys. Rev. Lett. **52**, 2285 (1984).

[6] H. A. Mook and J. W. Lynn, Measurements of the magnetic excitations above T_c in iron and nickel (invited), J. Appl. Phys. **57**, 3006 (1985).

[7] Z. Lin, J. H. Choi, Q. Zhang, W. Qin, S. Yi, P. Wang, L. Li, Y. Wang, H. Zhang, Z. Sun, L. Wei, S. Zhang, T. Guo, Q. Lu, J. H. Cho, C. Zeng, and Z. Zhang, Flatbands and emergent ferromagnetic ordering in Fe_3Sn_2 kagome lattices, Phys. Rev. Lett. **121**, 096401 (2018).

[8] X. Xu, Y. W. Li, S. R. Duan, S. L. Zhang, Y. J. Chen, L. Kang, A. J. Liang, C. Chen, W. Xia, Y. Xu, P. Malinowski, X. D. Xu, J.-H. Chu, G. Li, Y. F. Guo, Z. K. Liu, L. X. Yang, and Y. L. Chen, Signature for non-Stoner ferromagnetism in the van der Waals ferromagnet Fe_3GeTe_2, Phys. Rev. B **101**, 201104(R) (2020).

[9] Y. Zhang, H. Lu, X. Zhu, S. Tan, W. Feng, Q. Liu, W. Zhang, Q. Chen, Y. Liu, X. Luo, D. Xie, L. Luo, Z. Zhang, and X. Lai, Emergence of Kondo lattice behavior in a van der Waals itinerant ferromagnet, Fe_3GeTe_2, Sci. Adv. **4**, eaao6791 (2018).

[10] A. Nicolaou, M. Gatti, E. Magnano, P. Le Fèvre, F. Bondino, F. Bertran, A. Tejeda, M. Sauvage-Simkin, A. Vlad, Y. Garreau, A. Coati, N. Guérin, F. Parmigiani, and A. Taleb-Ibrahimi, Fermi surface symmetry and evolution of the electronic structure across the paramagnetic-helimagnetic transition in MnSi/Si(111), Phys. Rev. B **92**, 081110(R) (2015).

[11] Y. Fang, H. Zhang, D. Wang, G. Yang, Y. Wu, P. Li, Z. Xiao, T. Lin, H. Zheng, X.-L. Li, H.-H. Wang, F. Rodolakis, Y. Song, Y. Wang, C. Cao, and Y. Liu, Quasiparticle characteristics of the weakly ferromagnetic Hund metal MnSi, Phys. Rev. B **106**, L161112 (2022).

[12] A. Chikamatsu, H. Wadati, H. Kumigashira, M. Oshima, A. Fujimori, N. Hamada, T. Ohnishi, M. Lippmaa, K. Ono, M. Kawasaki, and H. Koinuma, Band structure and Fermi surface of $La_{0.6}Sr_{0.4}MnO_3$ studied by *in situ* angle-resolved photoemission spectroscopy, Phys. Rev. B **73**, 195105 (2006).

[13] L. L. Lev, J. Krempaský, U. Staub, V. A. Rogalev, T. Schmitt, M. Shi, P. Blaha, A. S. Mishchenko, A. A. Veligzhanin, Y. V. Zubavichus, M. B. Tsetlin, H. Volfová, J. Braun, J. Minár, and V. N. Strocov, Fermi surface of three-dimensional $La_{1-x}Sr_xMnO_3$ explored by soft-X-Ray ARPES: Rhombohedral lattice distortion and its effect on magnetoresistance, Phys. Rev. Lett. **114**, 237601 (2015).

[14] A. Georges, L. de' Medici, and J. Mravlje, Strong correlations from Hund's coupling, Annu. Rev. Condens. Matter Phys. **4**, 137 (2013).

[15] Y. Nomura, S. Sakai, and R. Arita, Fermi surface expansion above critical temperature in a Hund ferromagnet, Phys. Rev. Lett. **128**, 206401 (2022).

[16] M. Brando, D. Belitz, F. M. Grosche, and T. R. Kirkpatrick, Metallic quantum ferromagnets, Rev. Mod. Phys. **88**, 025006 (2016).

[17] G. R. Stewart, Unconventional superconductivity, Adv. Phys. **66**, 75 (2017).

[18] A. Callaghan, C. W. Moeller, and R. Ward, Magnetic interactions in ternary ruthenium oxides, Inorg. Chem. **5**, 1572 (1966).

[19] J. M. Longo, P. M. Raccah, and J. B. Goodenough, Magnetic properties of $SrRuO_3$ and $CaRuO_3$, J. Appl. Phys. **39**, 1327 (1968).

[20] M. K. Crawford, R. L. Harlow, W. Marshall, Z. Li, G. Cao, R. L. Lindstrom, Q. Huang, and J. W. Lynn, Structure and magnetism of single crystal $Sr_4Ru_3O_{10}$: A ferromagnetic triple-layer ruthenate, Phys. Rev. B **65**, 214412 (2002).

[21] Z. Q. Mao, M. Zhou, J. Hooper, V. Golub, and C. J. O'Connor, Phase separation in the itinerant metamagnetic transition of $Sr_4Ru_3O_{10}$, Phys. Rev. Lett. **96**, 077205 (2006).

[22] S. A. Grigera, R. S. Perry, A. J. Schofield, M. Chiao, S. R. Julian, G. G. Lonzarich, S. I. Ikeda, Y. Maeno, A. J. Millis, and A. P. Mackenzie, Magnetic field-tuned quantum criticality in the metallic ruthenate $Sr_3Ru_2O_7$, Science **294**, 329 (2001).

[23] A. P. Mackenzie, S. R. Julian, A. J. Diver, G. J. McMullan, M. P. Ray, G. G. Lonzarich, Y. Maeno, S. Nishizaki, and T. Fujita, Quantum oscillations in the layered perovskite superconductor Sr_2RuO_4, Phys. Rev. Lett. **76**, 3786 (1996).

[24] A. P. Mackenzie and Y. Maeno, The superconductivity of Sr_2RuO_4 and the physics of spin-triplet pairing, Rev. Mod. Phys. **75**, 657 (2003).

[25] S.-C. Wang, H.-B. Yang, A. K. P. Sekharan, H. Ding, J. R. Engelbrecht, X. Dai, Z. Wang, A. Kaminski, T. Valla, T. Kidd, A. V. Fedorov, and P. D. Johnson, Quasiparticle line shape of Sr_2RuO_4 and its relation to anisotropic transport, Phys. Rev. Lett. **92**, 137002 (2004).

[26] T. Kondo, M. Ochi, M. Nakayama, H. Taniguchi, S. Akebi, K. Kuroda, M. Arita, S. Sakai, H. Namatame, M. Taniguchi, Y. Maeno, R. Arita, and S. Shin, Orbital-dependent band narrowing revealed in an extremely correlated Hund's metal emerging on the topmost layer of Sr_2RuO_4, Phys. Rev. Lett. **117**, 247001 (2016).

[27] T. Oguchi, Electronic band structure of the superconductor Sr_2RuO_4, Phys. Rev. B **51**, 1385 (1995).

[28] T. Yokoya, A. Chainani, T. Takahashi, H. Ding, J. C. Campuzano, H. Katayama-Yoshida, M. Kasai, and Y. Tokura, Angle-resolved photoemission study of Sr_2RuO_4, Phys. Rev. B **54**, 13311 (1996).

[29] A. V. Puchkov, Z.-X. Shen, and G. Cao, Electronic band structure of $Sr_3Ru_2O_7$, Phys. Rev. B **58**, 6671 (1998).

[30] A. Damascelli, D. H. Lu, K. M. Shen, N. P. Armitage, F. Ronning, D. L. Feng, C. Kim, Z.-X. Shen, T. Kimura, Y. Tokura, Z. Q. Mao, and Y. Maeno, Fermi surface, surface states, and surface reconstruction in Sr_2RuO_4, Phys. Rev. Lett. **85**, 5194 (2000).

[31] R. A. Borzi, S. A. Grigera, R. S. Perry, N. Kikugawa, K. Kitagawa, Y. Maeno, and A. P. Mackenzie, de Haas–van Alphen effect across the metamagnetic transition in $Sr_3Ru_2O_7$, Phys. Rev. Lett. **92**, 216403 (2004).

[32] A. Tamai, M. P. Allan, J. F. Mercure, W. Meevasana, R. Dunkel, D. H. Lu, R. S. Perry, A. P. Mackenzie, D. J. Singh, Z.-X. Shen, and F. Baumberger, Fermi surface and van Hove singularities in the itinerant metamagnet $Sr_3Ru_2O_7$, Phys. Rev. Lett. **101**, 026407 (2008).

[33] M. Malvestuto, E. Carleschi, R. Fittipaldi, E. Gorelov, E. Pavarini, M. Cuoco, Y. Maeno, F. Parmigiani, and A.

Vecchione, Electronic structure trends in the $Sr_{n+1}Ru_nO_{3n+1}$ family (n=1,2,3), Phys. Rev. B **83**, 165121 (2011).

[34] C. N. Veenstra, Z.-H. Zhu, B. Ludbrook, M. Capsoni, G. Levy, A. Nicolaou, J. A. Rosen, R. Comin, S. Kittaka, Y. Maeno, I. S. Elfimov, and A. Damascelli, Determining the surface-to-bulk progression in the normal-state electronic structure of Sr_2RuO_4 by angle-resolved photoemission and density functional theory, Phys. Rev. Lett. **110**, 097004 (2013).

[35] V. Sunko, E. Abarca Morales, I. Marković, M. E. Barber, D. Milosavljević, F. Mazzola, D. A. Sokolov, N. Kikugawa, C. Cacho, P. Dudin, H. Rosner, C. W. Hicks, P. D. C. King, and A. P. Mackenzie, Direct observation of a uniaxial stress-driven Lifshitz transition in Sr_2RuO_4, npj Quantum Mater. **4**, 46 (2019).

[36] D. E. Shai, C. Adamo, D. W. Shen, C. M. Brooks, J. W. Harter, E. J. Monkman, B. Burganov, D. G. Schlom, and K. M. Shen, Quasiparticle mass enhancement and temperature dependence of the electronic structure of ferromagnetic $SrRuO_3$ thin films, Phys. Rev. Lett. **110**, 087004 (2013).

[37] S. Hahn, B. Sohn, M. Kim, J. R. Kim, S. Huh, Y. Kim, W. Kyung, M. Kim, D. Kim, Y. Kim, T. W. Noh, J. H. Shim, and C. Kim, Observation of spin-dependent dual ferromagnetism in perovskite ruthenates, Phys. Rev. Lett. **127**, 256401 (2021).

[38] H. F. Yang, Z. T. Liu, C. C. Fan, Q. Yao, P. Xiang, K. L. Zhang, M. Y. Li, H. Li, J. S. Liu, D. W. Shen, and M. H. Jiang, Origin of the kink in the band dispersion of the ferromagnetic perovskite $SrRuO_3$: Electron-phonon coupling, Phys. Rev. B **93**, 121102(R) (2016).

[39] E. K. Ko, S. Hahn, C. Sohn, S. Lee, S.-S. B. Lee, B. Sohn, J. R. Kim, J. Son, J. Song, Y. Kim, D. Kim, M. Kim, C. H. Kim, C. Kim, and T. W. Noh, Tuning orbital-selective phase transitions in a two-dimensional Hund's correlated system, Nat. Commun. **14**, 3572 (2023).

[40] R. Matzdorf, Z. Fang, Ismail, J. Zhang, T. Kimura, Y. Tokura, K. Terakura, and E. W. Plummer, Ferromagnetism stabilized by lattice distortion at the surface of the p-wave superconductor Sr_2RuO_4, Science **289**, 746 (2000).

[41] Y. J. Jo, L. Balicas, N. Kikugawa, K. Storr, M. Zhou, and Z. Q. Mao, Shubnikov–de Haas effect across a metamagnetic transition in high quality single crystals of $Sr_4Ru_3O_{10}$, J. Phys.: Conf. Ser. **51**, 247 (2006).

[42] P. Ngabonziza, E. Carleschi, V. Zabolotnyy, A. Taleb-Ibrahimi, F. Bertran, R. Fittipaldi, V. Granata, M. Cuoco, A. Vecchione, and B. P. Doyle, Fermi surface and kink structures in $Sr_4Ru_3O_{10}$ revealed by synchrotron-based ARPES, Sci. Rep. **10**, 21062 (2020).

[43] C. A. Marques, P. A. E. Murgatroyd, R. Fittipaldi, W. Osmolska, B. Edwards, I. Benedičič, G.-R. Siemann, L. C. Rhodes, S. Buchberger, M. Naritsuka, E. Abarca-Morales, D. Halliday, C. Polley, M. Leandersson, M. Horio, J. Chang, R. Arumugam, M. Lettieri, V. Granata, A. Vecchione *et al.*, Spin-orbit coupling induced Van Hove singularity in proximity to a Lifshitz transition in $Sr_4Ru_3O_{10}$, npj Quantum Mater. **9**, 35 (2024).

[44] M. Zhou, J. Hooper, D. Fobes, Z. Mao, V. Golub, and C. O'Connor, Electronic and magnetic properties of triple-layered ruthenate $Sr_4Ru_3O_{10}$ single crystals grown by a floating-zone method, Mater. Res. Bull. **40**, 942 (2005).

[45] M. Kitamura, S. Souma, A. Honma, D. Wakabayashi, H. Tanaka, A. Toyoshima, K. Amemiya, T. Kawakami, K. Sugawara, K. Nakayama, K. Yoshimatsu, H. Kumigashira, T. Sato, and K. Horiba, Development of a versatile micro-focused angle-resolved photoemission spectroscopy system with Kirkpatrick–Baez mirror optics, Rev. Sci. Instrum. **93**, 033906 (2022).

[46] G. Kresse and J. Furthmüller, Efficient iterative schemes for *ab initio* total-energy calculations using a plane-wave basis set, Phys. Rev. B **54**, 11169 (1996).

[47] M. Kawamura, FermiSurfer: Fermi-surface viewer providing multiple representation schemes, Comput. Phys. Commun. **239**, 197 (2019).

[48] S. Ideta, K. Takashima, M. Hashimoto, T. Yoshida, A. Fujimori, H. Anzai, T. Fujita, Y. Nakashima, A. Ino, M. Arita, H. Namatame, M. Taniguchi, K. Ono, M. Kubota, D. H. Lu, Z.-X. Shen, K. M. Kojima, and S. Uchida, Enhanced superconducting gaps in the trilayer high-temperature $Bi_2Sr_2Ca_2Cu_3O_{10+\delta}$ cuprate superconductor, Phys. Rev. Lett. **104**, 227001 (2010).

[49] D. J. Singh, Electronic and magnetic properties of the 4d itinerant ferromagnet $SrRuO_3$, J. Appl. Phys. **79**, 4818 (1996).

[50] S.-I. Ideta, T. Yoshida, A. Fujimori, H. Anzai, T. Fujita, A. Ino, M. Arita, H. Namatame, M. Taniguchi, Z.-X. Shen, K. Takashima, K. Kojima, and S.-I. Uchida, Energy scale directly related to superconductivity in high-T_c cuprates: Universality from the temperature-dependent angle-resolved photoemission of $Bi_2Sr_2Ca_2Cu_3O_{10+\delta}$, Phys. Rev. B **85**, 104515 (2012).

[51] S. Chikara, V. Durairaj, W. H. Song, Y. P. Sun, X. N. Lin, A. Douglass, G. Cao, P. Schlottmann, and S. Parkin, Borderline magnetism in $Sr_4Ru_3O_{10}$: Impact of La and Ca doping on itinerant ferromagnetism and metamagnetism, Phys. Rev. B **73**, 224420 (2006).

[52] M. Imada, A. Fujimori, and Y. Tokura, Metal-insulator transitions, Rev. Mod. Phys. **70**, 1039 (1998).

[53] T. J. Kreutz, T. Greber, P. Aebi, and J. Osterwalder, Temperature-dependent electronic structure of nickel metal, Phys. Rev. B **58**, 1300 (1998).